Progress in Natural Science: Materials International 26 (2016) 117–128

HOSTED BY

Contents lists available at ScienceDirect

Progress in Natural Science: Materials International

journal homepage: www.elsevier.com/locate/pnsmi

Effect of long-period stacking ordered phase on microstructure, mechanical property and corrosion resistance of Mg alloys: A review

Daokui Xu [a], En-hou Han [a,*], Yongbo Xu [a,b]

[a] Environmental Corrosion Center, Institute of Metal Research, Chinese Academy of Sciences, 62 Wencui Road, Shenyang 110016, China
[b] Shenyang National Laboratory for Materials Science, 72 Wenhua Road, Shenyang 110016, China

ARTICLE INFO

Article history:
Received 27 October 2015
Accepted 15 January 2016
Available online 20 April 2016

Keywords:
Mg alloys
Long-period stacking ordered structure
Microstructural characterization
Mechanical properties
Corrosion resistance

ABSTRACT

Magnesium alloys containing long period stacking ordered (LPSO) phase have been received a great deal of attention in the last decade owing to their excellent comprehensive properties of mechanical strength and corrosion resistance. In this paper, some fundamental aspects of LPSO containing Mg alloys have been reviewed, including: (1) microstructural characterization, formation conditions and the associated phase transformation of LPSO phases in Mg alloys; (2) deformation mechanism of LPSO phases and their influence on the deformation mechanism of the Mg matrix; (3) effect of LPSO structure on the mechanical performance such as tensile strength, creep resistance, fracture toughness and fatigue strength; (4) corrosion behavior of LPSO containing Mg alloys and their possible applications as the biomaterials. Moreover, some remaining unsolved issues of the LPSO containing Mg alloys and the future target about how to further improve their service properties have been also described.

1. Introduction

Magnesium alloys are of great interest as the lightweight structural materials for many potential applications including transportation, aerospace and electric communication as well as medical device and so on. In particular, Mg alloys containing long period stacking ordered (LPSO) structure received considerable concerns in the last decade due to their good combined properties of mechanical strength and corrosion resistance [1–3]. At the beginning of the 21st century, Kawamura et al. reported that the tensile yield strength and elongation of a $Mg_{97}Zn_1Y_2$ (at%) alloy prepared by rapid solidification processing and hot extrusion can reach 610 MPa and ~5%, respectively [1,4]. These excellent mechanical properties are ascribed to the dispersed nano-scale long period stacking ordered (LPSO) phases [2]. Since then, this kind of novel structure has raised a great enthusiasm for researching the LPSO phases in Mg alloys and their effect on the mechanical performance. Actually, Luo et al. observed the X-phase, an 18R modulated structure with a period of 4.68 nm in Mg–Zn–Zr–RE (RE=rare earth element) alloy as early as 1994 [5,6], which was later designated as 18R-LPSO phase [5–9]. After that, researchers also observed 18R-, 14H-, 10H-and 23R-LPSO structures in Mg–TM–RE (TM=Zn, Cu, Ni; RE=Y, La, Ce, Pr, Sm, Nd, Dy, Ho, Er, Gd and Tm) alloys. More recently, three new types of 15R-, 12H-and 21R-LPSO structures were also found in an as-cast Mg–Co–Y alloy [10]. These various LPSO phases in Mg–M (M=Zn, Cu, Ni and Co)-RE alloys were characterized by using transmission electron microscopy (TEM) techniques, such as electron diffraction pattern (EDP) [5,8,10–12], energy dispersion X-ray spectroscopy (EDX) [11], convergent-beam electron diffraction (CBED) [13], and high-angle annular dark field scanning transmission electron microscopy (HAADF-STEM) [2,10–14].

Due to the complexity of the LPSO structures, their effects on the mechanical properties and corrosion resistance have been widely investigated in different kinds of Mg-based alloys [3,15–19]. It demonstrated that the LPSO phase can strengthen the alloys without sacrificing the ductility. Meanwhile, the existence of the LPSO phase can retain the strength of Mg alloys during the hot deformation, and then enhance their creep resistance. In addition, LPSO containing Mg-alloys exhibit a better corrosion resistance when compared to the conventional Mg alloys such as AZ31, WE43, ZK60 and ZX60.

In this paper, the current understanding about the microstructure, phase transformation and deformation mechanisms of the LPSO structure in Mg alloys and their effects on the mechanical properties at both room and elevated temperatures and corrosion behavior of Mg alloys are reviewed.

* Corresponding author.
E-mail address: ehhan@imr.ac.cn (E.-h. Han).
Peer review under responsibility of Chinese Materials Research Society.

http://dx.doi.org/10.1016/j.pnsc.2016.03.006

2. Structure of LPSO phase

2.1. Stacking and chemical ordered LPSO structures

Generally, LPSO structures in Mg alloys mainly exist in the form of a three-dimensional quasi-continuous honeycomb-like network at grain boundaries [13], as shown in Fig. 1. These LPSO phases are not only stacking ordered but also chemical ordered [2,11–14]. According to their different stacking sequences, so far, four types of LPSO structures including 10H, 18R, 14H and 24R have been reported in Mg–M–RE systems (M=Al, Ni, Cu and Zn; RE=Y, Gd, Dy, Ho, Er, Tb and Tm). The LPSO phase was initially designated as 6H or 6H′ [2,20], which was subsequently considered to be incorrect and replaced by 18R. Fig. 2 shows that the stacking sequences of these LPSO phases along the *c*-axis contain an AB′C′A-type building block [12]. More recently, Mi et al. reported that the other three kinds of LPSO structures, i.e. 15R, 12H and 21R exist in an as-cast Mg–Co–Y alloy [10]. Moreover, the stacking sequence of these LPSO structures includes an AB′C-type building block. For comparison, all of the LPSO structures in Mg alloys observed so far are summarized in Table 1, where the layers denoted by a prime are enriched with M/RE atoms [21]. Obviously, two atomic planes are enriched with heavier atoms in the 10H-, 18R-, 14H-and 24R-LPSO structures, while one atomic layer exists in the 15R-, 12H-and 21R-LPSO structures. In addition, there are 1–4 layers of Mg sandwiched in the AB′C′A-type building block for the former types of LPSO phases, while 2–4 layers of Mg sandwiched in the AB′C-type building block for the latter types of LPSO phases. These significant features of LPSO structures are possibly related to the intrinsic electronic structure of the M elements.

Besides the stacking and chemical ordering of the LPSO phase along the basal plane, the in-plane ordering of solute elements has attracted increasing attention. The features of in-plane ordering or disordering of M-RE clusters are crucial for understanding the stability and formation of LPSO structures in Mg-based ternary alloys because they can influence and even determine the allowable range of composition and stoichiometry for the formed LPSO phases [22]. Zhu et al. [11] disclosed the existence of in-plane ordering of Zn and Y atoms in two consecutive close-packed atomic planes in 18R and 14H LPSO phases in Mg–Zn–Y ternary and proposed a modeling crystal structure containing an ordered arrangement of Zn and Y atoms. However, the diffuse streaks taken from 18R-and 14H-LPSO phases in the Mg–M–RE ternary systems may imply a disordered nature of the structure rather than the long-range ordered structure. Yokobayashi et al. demonstrated that the in-plane ordering of Gd (and possibly Al) atoms in the close-packed atomic planes in the LPSO phase of Mg–Al–Gd alloys, where the enrichment of Gd and Al atoms are expected to occur in order to fully describe the crystal structure of the LPSO phase [23]. Fig. 3 shows that the Gd atoms (or Al) actually exhibit long-range ordered arrangements in-plane in the quadruple enriched close-packed planes [23]. Obviously, the enrichment of RE and M atoms is in the four (not two) consecutive planes, which is different from the atomic model proposed in Mg–Zn–Y alloys [11]. As for the LPSO phase in Mg–Zn–Y alloys, a well-annealed $Mg_{85}Zn_6Y_9$ (at%) alloy was firstly observed to show weak but clear local $L1_2$-type in-plane short ordering [24]. Kimizuka et al. explained the fully ordered and local short range ordered TM_6RE_8 in Mg–Al–Gd and Mg–Zn–Y alloys via DTF [22]. More recently, Yamasaki et al. [25] observed that the degree of order for the 10H-LPSO Mg–Zn–Y phase, formed in $Mg_{75}Zn_{10}Y_{15}$ (at%) alloys annealed at 773 K, is similar to that of the Mg–Al–Gd alloys. Obviously, the spots in all of three SAED patterns became sharper after annealing, indicating that the degree of order of the LPSO phase in Mg–Zn–Y alloys is changed by heat treatment. Moreover, the HAADF-STEM image demonstrates that the highest in-plane order exists in the 10H-LPSO phase of Mg–Zn–Y alloy. As for Mg–Co–Y alloy, the in-plane order of LPSO phases is still unclear. Any SAED patterns of 15R, 12H, or 21R do not show extra diffuse diffractions and/or weak streaks along the c^* direction as observed in the LPSO structure of Mg–Zn–RE alloys, implying that the Co/Y chemical order may not occur within the close-packed planes [10].

2.2. Formation, transformation and coexistence of LPSO structure

Generally, 18R-LPSO phase forms at the grain boundaries as a secondary phase during solidification, whereas 14H-LPSO phase precipitates during heat treatment at elevated temperatures after casting [15]. Their formation could be ascribed to different methods, such as, the rapidly solidified/powder metallurgy [2,3,26,27], melt-spun [8,28,29], Cu-mold casting and induction melting [5,6,15,30,31] and conventional casting [3,32–34].

For the original formation region of LPSO phases, Matsuura et al. proposed a formation mechanism of LPSO in a Mg–Cu–Y alloy

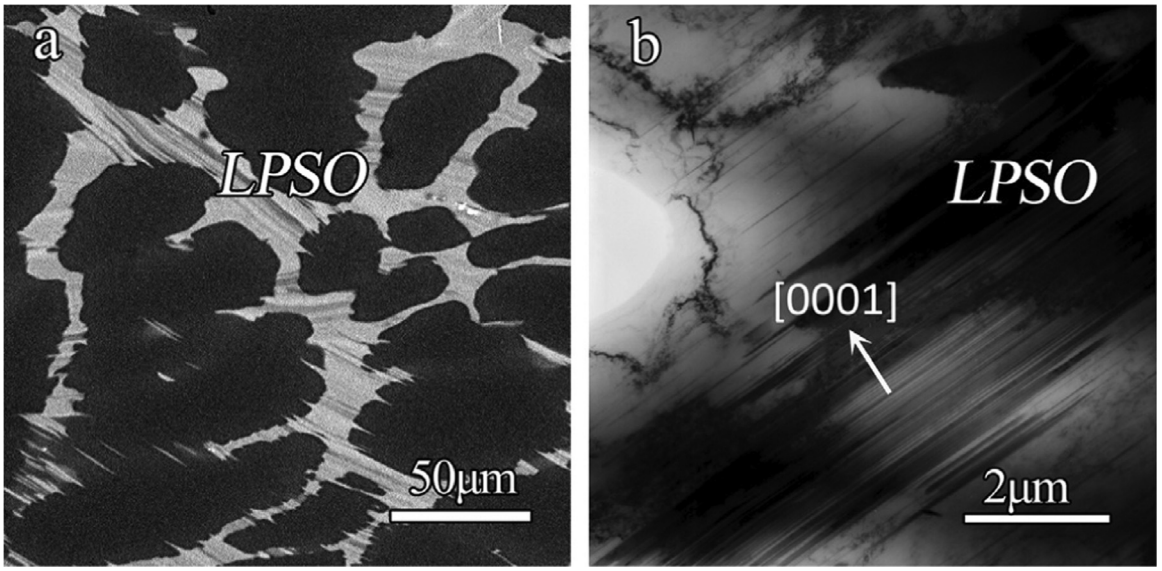

Fig. 1. (a) SEM images showing the general characteristics of the microstructures in as-cast $Mg_{97}Zn_1Y_2$ (at%) alloy; (b) low-magnification TEM image exhibiting salient features of the LPSO phase. Reproduced from Ref. [13].

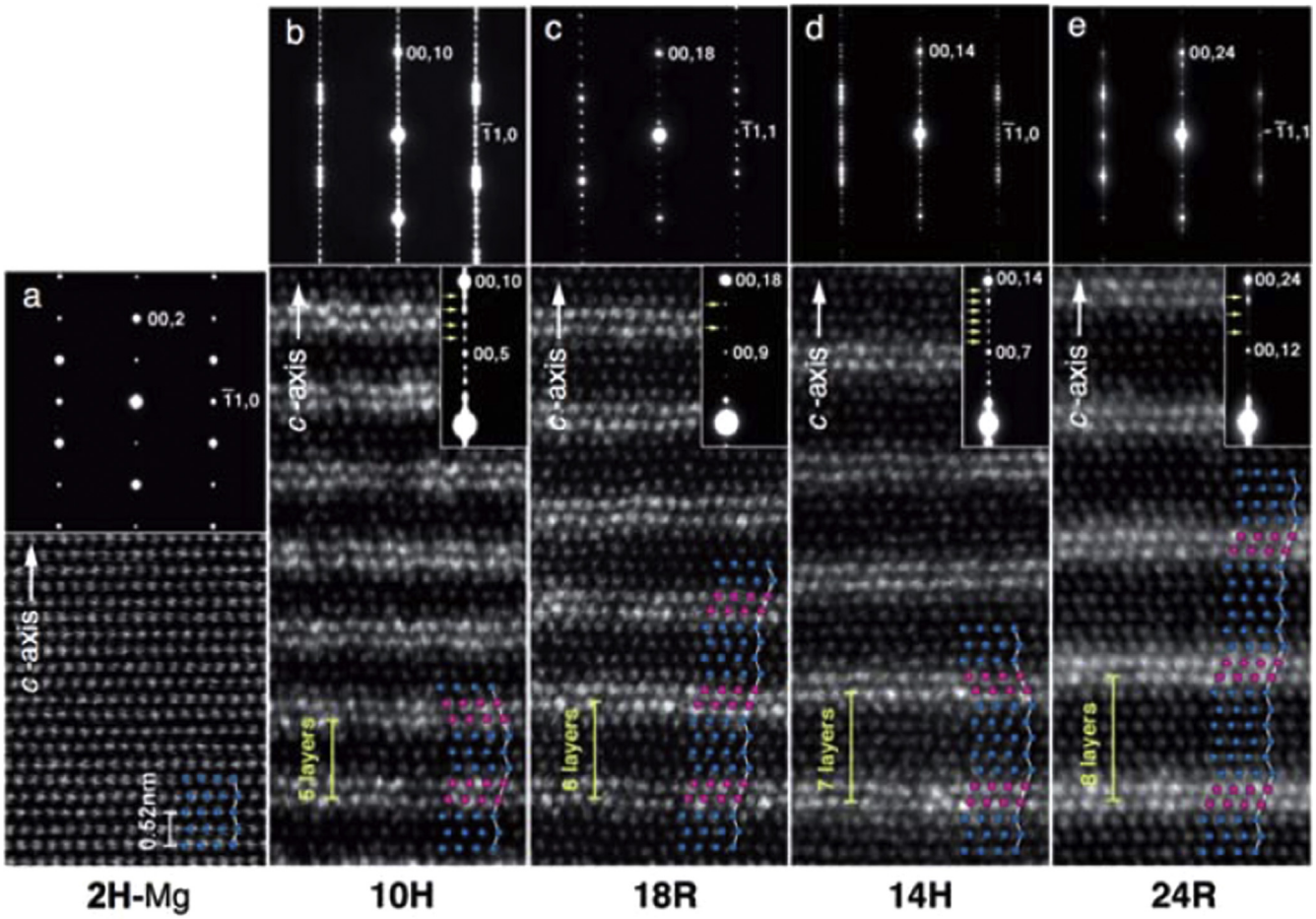

Fig. 2. Selected area electron diffraction (SAED) patterns and Z-contrast STEM images of (a) hcp-Mg and long-period stacking ordered structures of (b) 10H-type, (c) 18R-type, (d) 14H-type, and (e) 24R-type, respectively. Reproduced from Ref. [12].

Table 1
Stacking sequence of various LPSO phases in Mg–M–RE alloys [21].

LPSO	Stacking sequence along *c*-axis	Reference
10H	AB′C′ACAC′B′AB	
18R	AB′C′ACACA′B′CBCBC′A′BAB	[8]
14H	AB′C′ACACAC′B′ABAB	[12]
24R	AB′C′ACACACA′B′CBCBCBC′A′BABAB	
15R	AB′CBC BC′ACA CA′BAB	
12H	AB′CBCBCB′ABAB	[10]
21R	AB′CBCBC BC′ACACA CA′BABAB	

[35]. It mainly contains two steps, i.e., (1) the formation of an amorphous layer along the grain boundary and (2) the LPSO crystal growth from the boundary up to the inside of the Mg matrix crystal. It indicates that the LPSO crystals evolve and grow towards the Mg matrix by consuming the amorphous layer [35].

On the atomic level, LPSO structure is referred to the introduction of a new long-period ordered lattice in original crystal lattice period. Abe et al. reported [2] that the 6H′- (later denoted as 18R) type LPSO with ABCBCB stacking sequence forms from 2H hcp-Mg. It mainly includes two steps: (1) introduce the stacking faults on every six close-packed planes of 2H-Mg crystal, and (2) the segregation of solute atoms of Zn and Y around these stacking fault layers. The former is a stacking ordered process, which requires a propagation of Shockley partial dislocations, and the segregation of solute atoms of Zn and Y around these faults induced by the local strain field around the dislocations.

Zhu et al. observed the growth of LPSO phases and transformation between 18R and 14H phases in a Mg–8Y–2Zn–0.6Zr (wt%) alloy using TEM and atomic resolution HAADF-STEM [14]. The growth of both 18R and 14H within the α-Mg matrix occurs via a ledge mechanism, with the thickness of the particle increasing by the height of the ledge as it propagates. The unit height of the growth ledges or disconnections is 1.563 nm ($6 \times d_{(0002)Mg}$) for 18R and 1.824 nm ($7 \times d_{(0002)Mg}$) for 14H, and the displacement vector is $a/3 < 100 >_{\alpha}$ [14]. This mechanism is roughly analogous to that proposed by Abe et al. [2]. The 14H-LPSO phase is a thermodynamically stable structure and can still safely exist even after annealing at 773 K [7,11]. In agreement with experimental observations, DFT simulations disclose the transformation of the 18R LPSO structures to 14H [36].

Based on the observations to the microstructure of Mg–Y–Zn alloys during the prolonged heat treatment at 500 °C, the transformation mechanism from 18R-to 14H-LPSO phase was put forward [14]. Moreover, the transformation from 18R to 14H occurs most readily in the regions where the 18R structure is irregular in the building block stacking and the diffusion rate of Y and Zn atoms into the segregation layers controls the phase transformation.

Different from 18R-LPSO phase in Mg–Zn/Cu–Y alloy mentioned above, the 14H-LPSO phase in Mg–Zn–Gd alloys can not only precipitate from the supersaturated 2H-Mg matrix, but also can transform from Mg_3Gd-type compound phase during heat treatment [33]. Yamasaki et al. investigated the formation process of the LPSO in Mg–Zn–Gd alloys, and proposed a time-temperature transformation (TTT) diagram. At ~623 K, the 14H LPSO phase mainly precipitates and grows from highly dispersed stacking

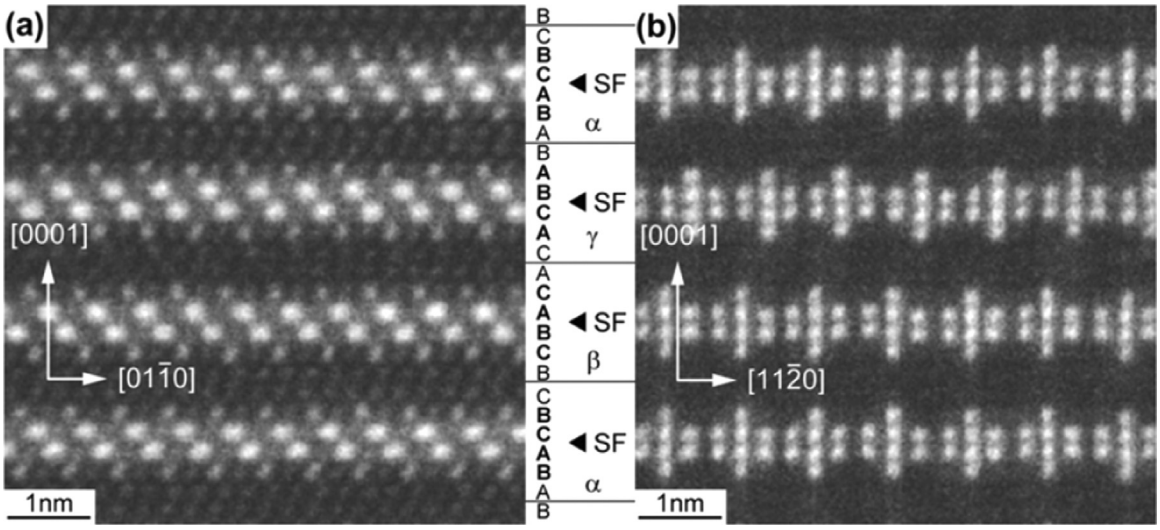

Fig. 3. Atomic resolution HAADF-STEM images of the Mg–Al–Gd LPSO phase taken along (a) and (b). Reproduced from Ref. [23].

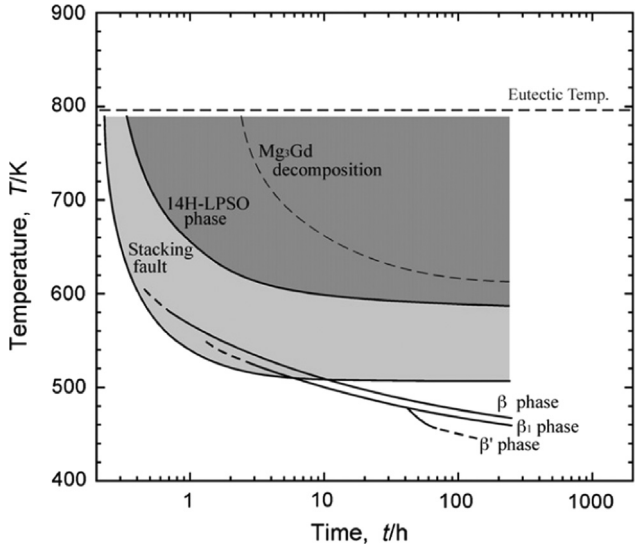

Fig. 4. Time–temperature transformation diagram for precipitation processes of β′, β1, β, SF, and 14H-LPSO in $Mg_{97}Zn_1Gd_2$ alloy. Reproduced from Ref. [33].

faults [33]. When the temperature is in the temperature range 723–773 K, the 14H LPSO phase forms as block-like shapes from the decomposition of Mg_3Gd. Fig. 4 shows the precipitation processes of the $Mg_{97}Zn_1Gd_2$ alloy as shown in the TTT diagram [33], indicating that the formation of β′, β1, β, SF and 14H-LPSO is dependent on the temperature and holding time.

A number of observations demonstrate that the coexistence and transformation of LPSO structures may take place in a number of the Mg–TM–RE alloys [8,7,11,13]. Matsuda et al. [8] have found the coexistence of four types of 18R-, 14H-, 10H-and 24R-LPSO structures in a rapid solidified $Mg_{97}Zn_1Y_2$ alloy followed by annealing at 573 K for 3.6 ks. These types of LPSO structures can be observed not only in the same specimen, but also in the same grain. Additionally, no differences in their morphologies and formation sites can be observed. Usually, the 18R structure can be transformed into 14H structure after heat treatment at a certain temperature [15]. Thus, 18R and 14H structures should be able to coexist with each other under some situations. Based on the Calphad-type thermodynamic calculations about Mg–Zn–Y system alloys [37], it demonstrated that the 18R and 14H structures could stably coexist in the temperature range from 483 to 537 °C. In previous work, Shao et al. found that the 18R- and 14H-LPSO structures could grow alternatively in a Mg-Zn-Y alloy after holding at 500 °C for 5 h [38]. Moreover, the difference in stacking sequence between 18R- and 14H-LPSO phases is that there are two or three Mg atomic layers between the two adjacent ABCA-fcc stacking units. Furthermore, the insertion of several Mg layers between the LPSO phases can result in the stacking faults in the LPSO structures [13]. This is consistent with the results observed in Mg–8Y–2Zn–0.6Zr (wt%) alloy [14].

Occasionally, the transformation from 14H structure into 18R structure can also be observed in the $Mg_{83}Ni_6Zn_5Y_6$ alloy after high temperature annealing at 673 or 773 K [39]. This opposite phase transformation is probably ascribed to the addition of Ni and content of alloying elements. However, so far, no relevant explanation can be referred. Thus, the effect of chemical compositions on the stability and phase transformation of LPSO structures still needs to be further investigated.

2.3. Effect of element addition on the formation and microstructure of LPSO structures

2.3.1. Additions and atomic ratio of alloying elements

It should be noticed that the previous studies about LPSO structures in Mg-alloys are mainly focused on Mg–Zn–RE system. Inoue et al. [27] report that there are no LPSO structure in the melt-spun alloys in ternary of Mg–Al–Y, and binary of Mg–Y and Mg–Zn, but the addition of Zn into Mg–Y can lead to 6H LPSO phase formation. The same result has been also reported by Gao et al. [31]. However, Apps et al. have found that LPSO phases can hardly exist in Mg–Y–Nd, Mg–Dy–Nd and Mg-Gd-Nd system alloys, and this is attributed to the absence of the plane faults in these alloys [39]. The addition of Zn makes a remarkable decrease of stacking fault energy (SFE) of the basal plane and Y stabilizes the long periodicity of LPSO phases [40]. Thus, it seems that the elements of Zn and RE are indispensable solute elements for the formation of the LPSO phases in Mg-RE system alloys. Moreover, Yamada et al. demonstrated that there was a definite content range of Zn addition for the formation of the LPSO in the Mg–Gd–Y–Zn–Zr alloys, and no LPSO phase could be formed when the content of Zn in the alloy was low than 0.3% or higher than 1.0% [34].

Afterwards, LPSO structures were also observed in other Mg-M-RE alloys, such as Mg–Y–Cu [3], Mg–Y–Ni [26,41], Mg–Al–Gd [42] and Mg–Co–Y [10]. Fig. 5 shows that LPSO phases can be formed in

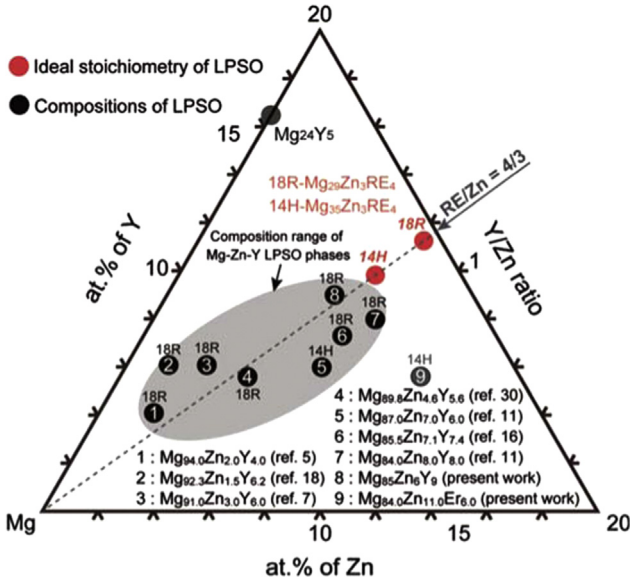

Fig. 5. Schematic quasi-isothermal section of the Mg–Zn–Y ternary phase diagram. Experimentally determined compositions of the Mg–Zn–Y LPSO phases [2,7,11,20,43,44] annealed at temperatures of 573–793 K are plotted together with the ideal stoichiometry compositions of the present LPSO models (red). 14H-Mg83Zn11Er6 is also plotted as no. 9 for comparison. Reproduced from Ref. [24].

the Mg–Zn–Y ternary systems with non-stoichiometric compositions and the Zn/Y atomic ratio is required to be less than 1 [2,7,11,20,24,43,44], suggesting that the LPSO phases could tolerate a considerable degree of disorder at the Zn and RE sites with statistical co-occupation by Mg, and thus the degree of order of the LPSO phases depends on the occupation conditions at the Zn/RE sites [24]. Moreover, the local atomic substitution behavior in the LPSO phases were deeply discussed in terms of the formation conditions of the Zn6RE8 clusters, and qualitatively explained about why the non-stoichiometric composition range was bounded by a fixed Zn/Y ratio [24].

2.3.2. Mixing enthalpy and atomic radius

As for Mg–Zn–RE (Y, La, Ce, Pr, Sm, Nd, Gd, Dy, Ho, Er, Tb, Tm and Yb) alloys, Kawamura et al. proposed a criteria for RE that could participate in the formation of LPSO phases [15]. The criteria mainly includes the following aspects [15]: (1) negative mixing enthalpy for Mg–RE and Zn–RE pairs, (2) HCP structure at room temperature, (3) large solid solubility limits above approximately 3.75 at% in magnesium, and (4) larger atomic size than Mg by 8.4–11.9%. After the observation of LPSO phases in Mg–Co–Y alloy, the above criteria were specified in Mg–TM–RE ternary systems. The mixing enthalpy between Mg–TM, Mg–RE should be −4 to 3 kJ/mol and −38 to −22 kJ/mol, respectively. Additionally, the atomic diameter of TM should be 0.124–0.143 nm [21].

Recently, Saal et al. examined the thermodynamic stability of these LPSO precipitates with density functional theory (DFT), and predicted the stabilities for 14H-and 18R-LPSO structures for many Mg–X_L–X_S ternary systems, where X_L and X_S were elements larger and smaller than Mg, respectively [45]. The stability of LPSO phase in 85 kinds of Mg–RE–X_S and 55 types of Mg–X_L–X_S ($X_L \neq RE$) ternary systems are summarized in Fig. 6. Here, the experimentally observed LPSO-formation systems were denoted by the symbol of "×" and the blue squares without a "×" indicated that the systems could be predicted the existence of stable LPSO phases. Moreover, it demonstrated that the favorable mixing energy between Mg and X_L on the fcc lattice and the size mismatch together served as the excellent criteria for determining the formation of X_L LPSO. Based

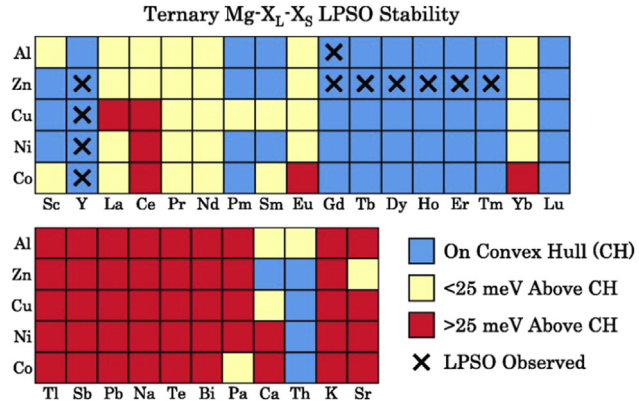

Fig. 6. Stability of 14H- and 18R-LPSO structures predicted by DFT, for all Mg–X_L–X_S ternary systems. X_S and X_L elements are given along the vertical and horizontal axes, respectively. Reproduced from Ref. [45].

on the criteria, the Ca-, Sr- and Th-containing LPSO structures are the most competitive with the ground state [45].

2.3.3. Impact of RE elements on the structural and chemical order of LPSO structures

Kawamura et al. reported that the LPSO phases were only observed in Mg–Zn–RE alloys with REs having a hexagonal closed packed (HCP) structure which is the same as Mg and Zn. The RE elements of non-LPSO Mg–Zn–RE alloys are hexagonal (HEX), face centered cubic (FCC), body centered cubic (BCC) or rhombic [15]. Therefore, it can be seen that the crystal structure of RE elements influences the formation of the LPSO phase.

2.3.4. Impact of TM elements on the structural and chemical order of LPSO structures

Generally, the 10H-, 14H-, 18R- and 24R-LPSO phases in Mg–TM–RE (TM = Ni, Cu, Al and Zn) alloys contain an ABCA-type building block, while the 15R-, 12H- and 21R-LPSO phases in Mg–Co–Y alloys include an ABC-type building block. The mixing enthalpy and atomic radius of these LPSO structures are summarized [8,10,11,21,23,46–48], as listed in Table 2. It can be seen that the difference in the mixing enthalpy of Mg–Co–Y is positive, while the others are negative. Thus, the mixing enthalpy between Mg–TM may be the critical factor affecting the stacking sequence of LPSO phases. Moreover, the atomic radius is possibly the key factor for determining the chemical order along basal plane of the alloys. Since the atomic radius of Al is almost the same as that of Zn, the

Table 2
Characteristics of metal elements and LPSO polytypes in Mg–TM–RE alloys [21].

Mg–TM–RE	Atomic radius of TM (nm)	Mixing enthalpy between Mg–TM (kJ/mol)	LPSO phases	Reference
Mg–Zn–Y	0.139	−4	10H, 14H, 18H, 24R	[8,11]
Mg–Cu–Y	0.128	−3	18R	[46]
Mg-Ni-Y	0.124	−4	18R	[46]
			14H, 18R-twin	[41]
			10H	[26]
Mg–Al–Gd	0.139	−2	18R	[23]
			14H	[47]
Mg–Co–Y	0.126	3	15R, 12H, 21R	[10]
			18R, 15R-twin, 18R-twin	[48]

LPSO phases in Mg-3.5 at% Al-5.0 at%Gd and Mg-10 at% Zn-15 at%Y alloys have the similar chemical order in basal planes. In contrast, the SAED patterns of LPSO phases in Mg-Co/Ni/Cu-Y indicated that the solute atoms could not arrange in order on basal planes, where the atomic radius of Co/Ni/Cu was smaller than that of Al/Zn. The possible reason is that the Al/Zn (0.139 nm) and Y/Gd (0.180 nm) pairs could better offset the induced strain due to the addition of solute elements.

So far, lots of research work has been focused on the microstructure characterization, formation mechanisms and stability of LPSO phases, but the key factors determining the intrinsic formation of the LPSO phases are still not well understood and need to be further investigated.

3. Deformation mechanisms of LPSO structures and its effect on twinning and dynamic recrystallization

3.1. Deformation kink

Deformation kink can be formed in the LPSO structures during various kinds of deformation [16,43,49,50]. The deformed microstructures of a $Mg_{97}Zn_1Y_2$ (at%) alloy with a compression strains of 23% (Sample 23%) and 60% (Sample 60%) under a strain rate of $10^{-3}\,s^{-1}$ at 573 K were observed, respectively. Obviously, the grains were elongated along the perpendicular directions with respect to the loading axis for both samples. Moreover, the multi-kinking bands could be observed and exhibited serrated morphology and kinking angle increased with increasing strain to up to 60% [16].

To understand the micro mechanism on the atomic scale about the deformation kinking of LPSO phases, TEM and HRTEM investigations were performed. TEM image of a deformation kink with relatively sharp and flat boundaries obtained in the Sample 23% revealed that the rotation angle was about 15° around $<1\bar{1}00>$ zone axis (inserted SAED Pattern). HRTEM images demonstrated that the boundaries of the deformation kink consisted of edge-type dislocations with a Burgers vector $b=\frac{1}{3}<11\bar{2}0>$ Obviously, the dislocations of the left and right KBs showed the opposite signs, i.e. the low angle kink bands were bounded by the opposite "tilt walls" of dislocations. Based on the HRTEM observations mentioned above, the synchronized slip of dislocations mechanism of kinking was deeply analyzed at the atomic scale [51,52].

Recently, Egusa et al. observed a micro-kinking feature occurred in the LPSO structures in a hot-extruded $Mg_{97}Zn_1Y_2$ alloy [53]. The kink boundaries were composed of multiply segmented kink-interfaces that were sequentially rotated with small angles in a definite direction. To explain this, schematic illustrations of kink deformation were proposed, as shown in Fig. 7. However, the micro-kinking mechanism can hardly be explained by the generation of dipole-pair dislocations in the early stage of kinking because this process can still occur when the grains were under multiple stress conditions such as shearing, bending, torsion and etc [53]. Therefore, further investigations are still needed to deeply clarify the microscopic mechanism of micro-kinking (rotational kinking) deformations.

3.2. Interaction between LPSO structures and deformation twinning

Due to the limited slip systems, the deformation twinning can play as one of the important deformation mechanisms in the metals and alloys with HCP structure. However, the formation of LPSO phases can inhibit the nucleation and growth of the deformation twinning [16,54,55]. For the $Mg_{97}Zn_1Y_2$ alloy tensile tested at room temperature, the dense LPSO phases can prevent

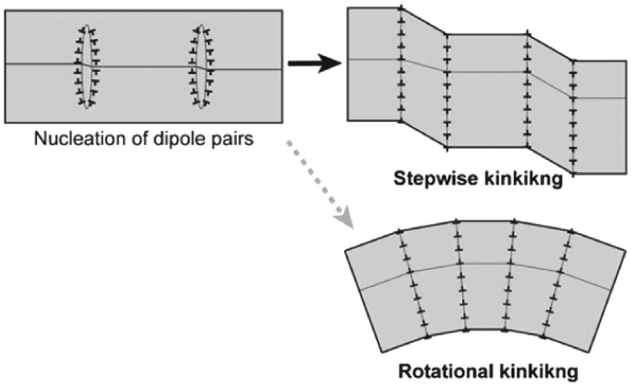

Fig. 7. Schematic illustrations of kink deformation: (left) nucleation of dislocation dipole pairs occurs within a grain interior. (Right-top) Dislocation walls moved apart and form sharp interfaces with a stepwise shape. (Right-bottom) Array of kink interfaces observed in the study. Reproduced from Ref. [53].

the growth of {10–12} deformation twinning in the α-Mg matrix, while the low density LPSO phases cannot inhibit the twinning activation [54]. Additionally, the interactions can exist between the deformation twin, LPSO structures and basal stacking faults (SFs). Previous work demonstrated that {10–12} twin can penetrate through SFs in the $Mg_{97}Zn_1Y_2$ alloy [55]. It is apparent that the interaction makes the misorientation angle of 84° between the basal planes of matrix and the twinned areas. This value slightly deviates from the misorientation due to the activation of an ideal {10-12} twinning. Meanwhile, the twin boundary is curved and deviated from the (10-12) habit plane and has a 4 nm wide waved ledge of severely distorted lattice contrast. Additionally, the deformation twin could re-orientate the SFs to the twinning orientation, but this process needs to pass through a relatively thick LPSO phase (~12 nm) under special deformation conditions. Furthermore, the reaction between deformation twin and basal SFs can not only lead to the formation of terraces along the basal planes in the twinned areas, but also can extend the severely distorted TBs. However, this case is slightly different from that of the fully coherent twin boundaries with periodic segregation of solute atoms in Mg-0.2 at%Gd, Mg-0.8 at%Gd, Mg-1.9 at%Zn and Mg-1.0 at%Gd-0.4 at% Zn-0.2 at% Zr alloys [56], which is due to the limited solute atoms existed in the α-Mg matrix compared with that of the $Mg_{97}Zn_1Y_2$ alloy.

3.3. Effect of LPSO structures on the dynamic recrystallization (DRX)

Generally, DRX is the result of rearrangement and/or annihilation of dislocations during high-temperature deformation processing. In the traditional compression or tensile tests performed at elevated temperatures, the LPSO phase can delay the occurrence of DRX due to its high thermal stability [57,58]. For example, only a very small volume fraction of DRX grains were observed in the Mg–Zn–Y alloys under compression at 573 K ($10^{-3}\,s^{-1}$) [16]. Furthermore, it has been reported that in Mg–2.0Zn–0.3Zr–5.8Y alloy, both 18R- and 14H-LPSO phases play an important role in delaying occurrence of the DRX under conditions of the temperature of 573–623 K and strain rate range of 0.001–0.01 s^{-1}, and the temperature 573–723 K and strain rate range of 0.1–1 s^{-1} [59,60]. The main reason can be ascribed to the retarding effect of the LPSO phase on the dislocation motion and migration of grain boundaries at high-temperatures. However, there still existed some large DRXed region in the Mg matrix for the hot-extruded Mg alloys performed at 623 K and 723 K [59,60]. Thus, the effect of LPSO structures on the DRX should be closely related to the deformation temperature and processing.

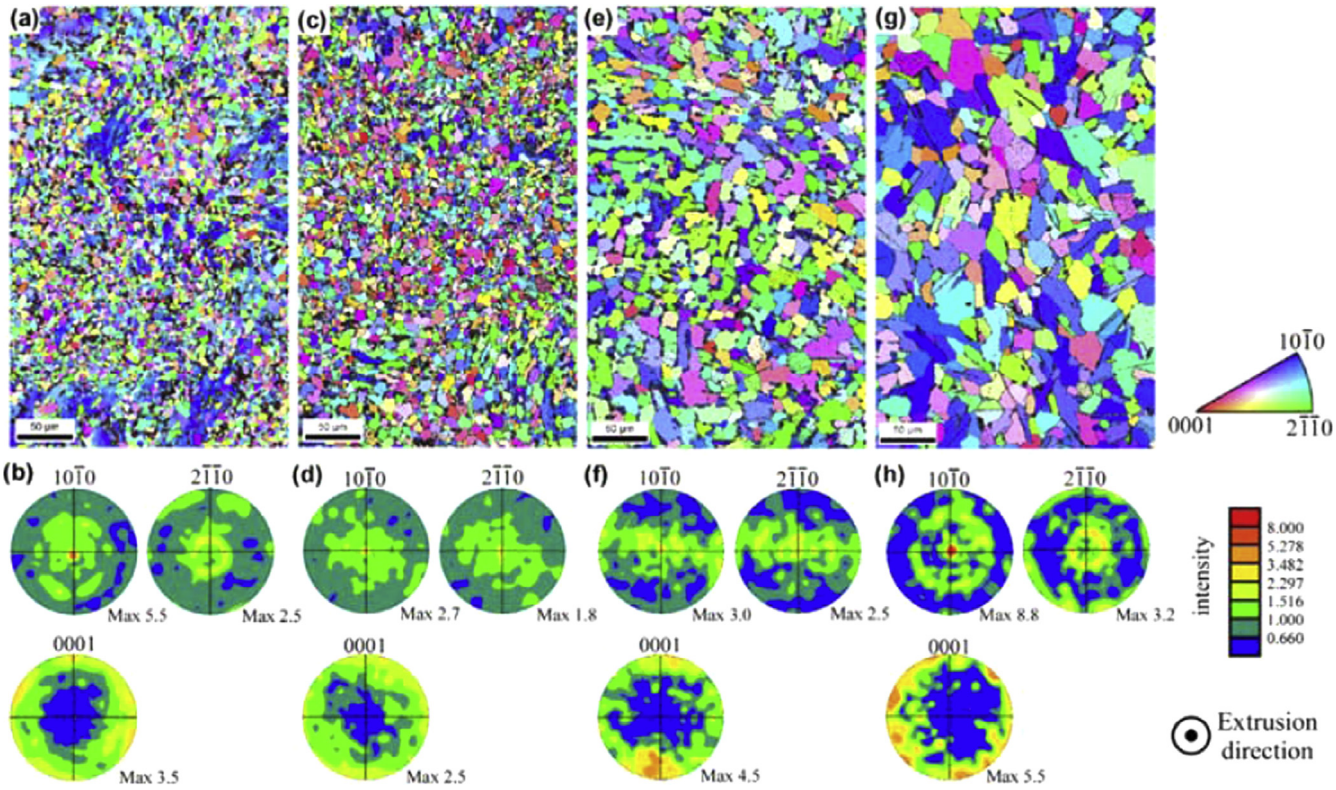

Fig. 8. Texture evolution of the Mg/LPSO alloy with different annealing temperatures: SEM-EBSD maps (a, c, e and g) and corresponding {10-10}, {11-20} and (0001) pole figures from the Mg-matrix grains: as-extruded (b) and annealed at 400 °C (d), 450 °C (f), and 475 °C (h). Reproduced from Ref. [50].

3.4. Texture evolution

Hagihara et al. compared the texture evolution of the $Mg_{97}Zn_1Y_2$ and $Mg_{99.2}Zn_{0.2}Y_{0.6}$ alloys annealed at different temperatures and found that grains in the LPSO containing $Mg_{97}Zn_1Y_2$ alloy exhibited a strong fiber texture [50], as shown in Fig. 8. It is worth to be noted that the intensity concentrations of the (0001) peak perpendicular to the extruded direction and that of {10-10} peak along the extruded direction in $Mg_{97}Zn_1Y_2$ alloy are considerably weaker than those of the conventional Mg alloys, meaning that the recrystallized grains in the LPSO-containing Mg alloy exhibit a randomized texture. However, after annealing at 400 °C, the intensity concentrations of (0001) peak perpendicular to the extrusion direction, and {10-10} peak along the extruded direction are weakened (Fig. 8(b)). However, during annealing at both 450 and 475 °C, these concentrations can be intensified, as shown in Fig. 8(c) and (d). Compared with these observations mentioned above, the basal fiber texture can be remarkably weakened during annealing at 400 °C and eliminated by annealing both at 450 and 475 °C for the Mg-solid solution $Mg_{99.2}Zn_{0.2}Y_{0.6}$ alloy [50]. It can be expected that the enhancement of the basal-fiber texture will be surely beneficial for improving the mechanical properties of the LPSO-containing Mg alloys. The yield stress of the as-extruded $Mg_{97}Zn_1Y_2$ alloy with strong basal texture can reach 270 MPa. Although the texture intensities of the alloy are slightly weakened after annealing at different temperatures, their strengths are still higher than those of $Mg_{99.2}Zn_{0.2}Y_{0.6}$ alloy. Later, Laser et al. further confirmed these results and found that the fiber texture of Mg–Ca–Ce alloys produced during extrusion may distinctly improve the strength of the Mg alloy [61]. More recently, Jono et al. reported the effect of LPSO phase-stimulated texture evolution on the creep resistance of extruded Mg–Zn–Gd alloys and found that the induced $<100>$ fiber textures can increase their creep strength [62].

4. Effect of LPSO structures on mechanical properties of Mg-alloys

4.1. Tensile properties at ambient and elevated temperatures of Mg alloys containing LPSO phase

Compared with the other commercial Mg alloys, LPSO-containing Mg alloys exhibit better mechanical properties. For example, the yield strength, tensile strength and elongation of a hot-extruded LPSO $Mg_{97}Y_2Cu_1$ alloy at ambient temperature are respectively 297 MPa, 377 MPa and 8.1%, whilst even at 473 K, these values can still be 273 MPa, 344 MPa and 16.3%, respectively [3]. When compared with that of the commercial Mg magnesium alloys, the strengths of the wrought LPSO-containing $Mg_{97}Y_2Cu_1$ alloy at room temperature are just slightly higher, but the alloy can exhibit remarkably higher strengths at elevated temperature [3,63], as shown in Fig. 9.

4.2. Compressive properties at room and elevated temperatures of LPSO containing Mg alloys

Besides the tensile properties, the LPSO-containing Mg alloys also have superior compressive properties [16,50,64]. When the compression tests were performed at the temperature of 573 K and strain rate of $10^{-3}\,s^{-1}$, the as-cast $Mg_{97}Zn_1Y_2$ alloy exhibited the highest peak stress of 190 MPa compared with pure Mg and commercial Mg alloys [16,65–69], as listed in Table 3. The reason can be mainly ascribed to the following three factors: (1) deformation kinking in LPSO phases play a key role in strengthening and toughening the Mg alloy; (2) the hardening LPSO phases have coherent interfaces with Mg matrix; and (3) LPSO phases inhibit the deformation twinning and delay the DRX [16].

Through investigating and comparing the compressive yield strengths of $Mg_{97}Zn_1Y_2$ extruded alloys containing with and

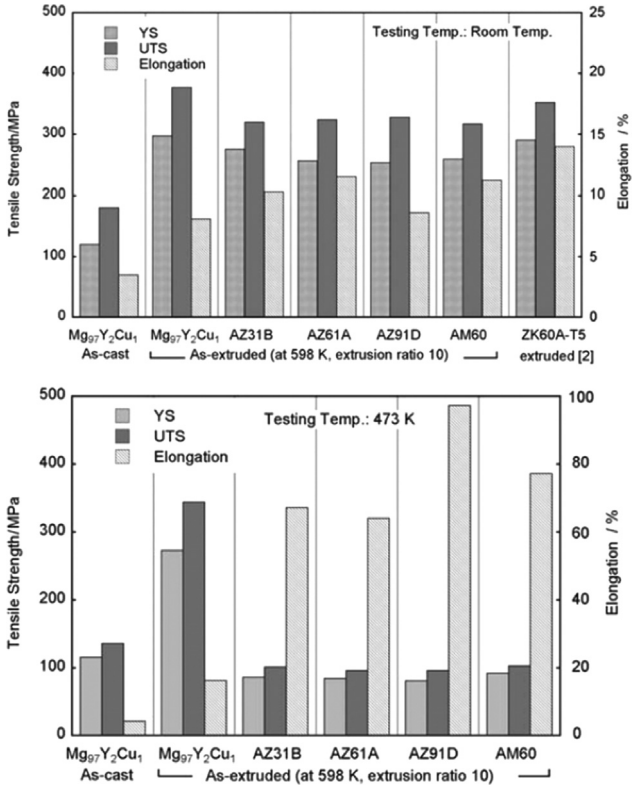

Fig. 9. Tensile properties of the hot-extruded $Mg_{97}Y_2Cu_1$ alloy compared with the as-cast $Mg_{97}Y_2Cu_1$ alloy at room temperature (a) and 473 K (b), and the extruded commercial Mg alloy [63] also included for comparison. Reproduced from Ref. [3].

Table 3
Comparison of the peak stresses of the Mg alloys tested in hot compression at 573 K [16].

Mg alloy	Peak stress/MPa	Strain rate/10^{-3} S^{-1}	Ref.
Pure Mg	30	1.7	[65]
Mg-0.035 at% Ce	60	1.7	[65]
AZ31	42	1.0	[66]
AZ91	79	1.0	[67]
ZK60	72	2.8	[68]
$Mg_{92}Zn_6Y_{1.5}Zr_{0.5}$	90	1.0	[69]
$Mg_{97}Zn_1Y_2$	190	1.0	[16]

without LPSO structures at room temperature, Hagihara et al. [50] reported that the yield stress of the alloy with a volume fraction 24% LPSO phase was higher than that of the LPSO phase-free alloy (3% LPSO phase) under all annealing conditions with the temperature ranging from 400 to 475 °C. For example, the yield stresses of the as-extruded $Mg_{97}Zn_1Y_2$ and $Mg_{99.2}Zn_{0.2}Y_{0.6}$ alloys were respectively 270 MPa and 140 MPa for the specimens with the annealing temperature of 400 and 475 °C [50]. And it has been observed that although the strengths decreased with increasing annealing temperature and time, the decreasing rate in yield stress for the $Mg_{97}Zn_1Y_2$ alloy was apparently lower than that of $Mg_{99.2}Zn_{0.2}Y_{0.6}$, indicating that the more LPSO phase containing Mg alloy can have good mechanical stability at elevated temperature due to the suppressing effect of LPSO phases on the grain growth. It has been found that the grain sizes of $Mg_{97}Zn_1Y_2$ alloy are much smaller than those of $Mg_{99.2}Zn_{0.2}Y_{0.6}$ alloys after annealing for about 200 h at both temperatures of 400 and 475 °C, indicating that the precipitation of LPSO structures in Mg alloys can decrease the grain size, and hence increase the compressive yield strengths.

Table 4
Variation of Vickers hardness with the volume fraction of LPSO phase in the alloys [18]

Alloy	%LPSO	HV
$MgY_3Zn_{1.5}$	35	84.7 ± 0.6
MgY_2Zn_1	21	82.5 ± 0.7
$MgY_1Zn_{0.5}$	9	65.4 ± 0.1

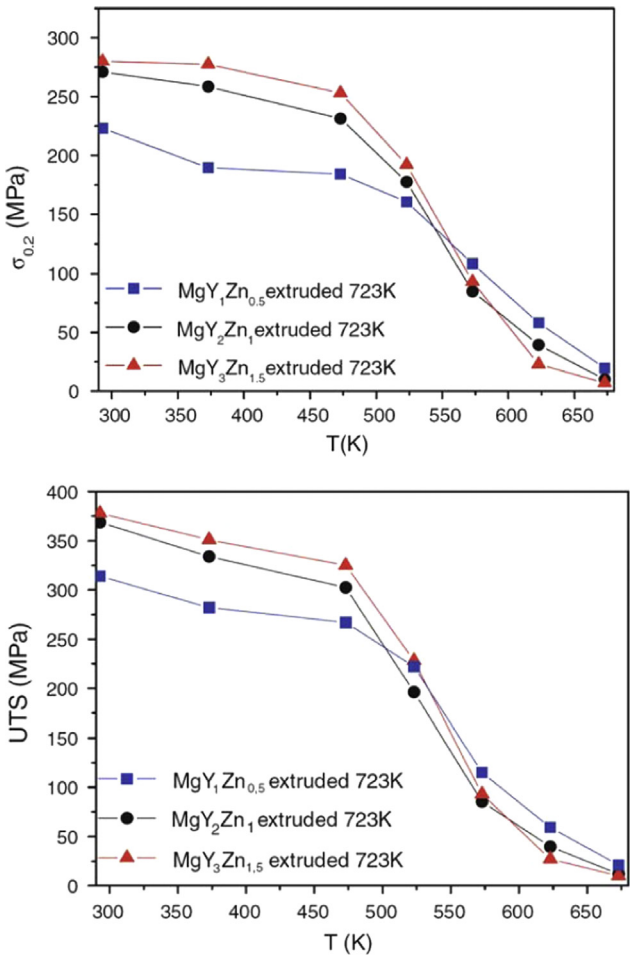

Fig. 10. Changes in Yield (a) and UTS (b) strengths as a function of the test temperature for the three alloys [18].

4.3. *Effect of volume fraction of LPSO phase on mechanical properties of Mg alloy*

Recently, Oñorbe et al. investigated the effect of the volume fraction of LPSO phase on the mechanical properties of three extruded $Mg_{100-3x}Y_{2x}Zn_x$ alloys (here $x = 0.5\%$, 1% and 1.5%) [18], and found that the volume fraction of LPSO phase increased with the increasing of both Y and Zn contents. The hardness variations of the alloys with the volume fraction of LPSO phase are listed in Table 4, showing that the hardness the alloys increased with the increment of the volume fraction of LPSO phase. Fig. 10 shows the dependence of yield stress and UTS on the testing temperature. It can be observed that for these three alloys, the yield stress and UTS values gradually decreases with the testing temperature increase, except a sharp decrease taking place at the temperature of 523 K. Although the mechanical strengths increase with the volume fraction of LPSO phase when the test temperature is lower than 523 K, the alloy ($MgY_1Zn_{0.5}$) with the lowest volume fraction of LPSO phase has higher yield and UTS values than those of other

Table 5
Ranges of strain rates and temperatures, creep exponent, and proposed creep mechanisms observed in the extruded $Mg_{97-3x}Y_{2x}Zn_x$ alloys [19].

High strain rates ($>10^{-4}\,s^{-1}$)	$n>10$	473–523 K (200–250 °C)	Load transfer mechanism
	$n\sim5$	573–623 K (300–350 °C)	Non-basal dislocation slip
	$n=3$	673 K (400 °C)	GBS
Intermediate strain rates ($10^{-4}\,s^{-1}-10^{-6}\,s^{-1}$)	$n\sim2$ to 3	573–673 K (300–400 °C)	GBS
Low strain rates ($>10^{-6}\,s^{-1}$)	$n>5$	573–673 K (300–400 °C)	GBS (threshold stress)

two alloys (MgY_2Zn_1 and $MgY_3Zn_{1.5}$) with higher volume fraction of LPSO phase when the test temperature is higher than 523 K. The reason for this may be related to the change of deformation mechanism of LPSO phases at the temperature higher than 523 K [18].

4.4. Effect of LPSO phase on creep behavior of Mg alloys

Generally, the LPSO-containing Mg–Zn–Y alloys can exhibit a high-stress exponent and high-activation energy at low-temperature and/or high strain rates. The superior creep resistance is originated from the LPSO-containing Mg alloys behaving as a metal matrix composite, where the Mg matrix can transfer part of loads to the LPSO phase [17]. Onorbe et al. reported that the creep resistance of LPSO-containing Mg alloys increased with the volume fraction of the contained LPSO phase [18]. Meanwhile, the alloys after heat treatment can still show the high creep resistance since the formed lamellar structure acts as an additional barrier against creep deformation [18]. To have a good understanding about the creep behavior of the LPSO-containing Mg alloys, the different dominant deformation mechanisms at different temperature and strain rates are summarized [19], as listed in Table 5.

4.5. Effect of LPSO phase on the fracture behavior of Mg alloys

In the investigation of the fracture behavior of Mg–Zn–Y alloys containing with different volume fractions of LPSO phases, Mine et al. demonstrated that the higher volume fraction of LPSO phases decreased the fracture toughness of Mg alloys [70]. For the $Mg_{97}Zn_1Y_2$ alloy, the calculated fracture toughness (K_{IC}) from the J-integral of the P–δ curves can reach 20–22 MPa at room temperature, which is higher than those of commercial heat-resistant AZ80 and WE54-T6 alloys (16 MPa in L-T orientation). In microfracture testing, the $Mg_{97}Zn_1Y_2$ alloy exhibited ductile fracture at 523 K, whereas it underwent brittle fracture at room temperature. For the $Mg_{88}Zn_5Y_7$ alloy, it shows a brittle P–δ response, irrespective of testing temperature.

4.6. Effect of LPSO phase on fatigue behavior of Mg alloys

So far, there has been a little work reported on the fatigue behavior of Mg alloys containing with LPSO phases. He et al. [71,72] reported the high-cycle fatigue behavior of the as-cast LPSO-containing Mg–Gd–Zn–Zr alloy and compared with that of the conventional Mg-based alloys, indicating that the fatigue strength of this alloy (105 MPa) is higher than those of the conventional Mg alloys (AZ91, AZ61, AM60 and ZE41) and even that of A356 Al alloy. Fig. 11 shows that the fatigue strengths after solution (T4) or solution and artificial aging (T6) can be improved to 112 and 130 MPa, respectively.

5. Corrosion behavior of LPSO phase containing Mg alloys

So far, lots of research works demonstrated the LPSO containing

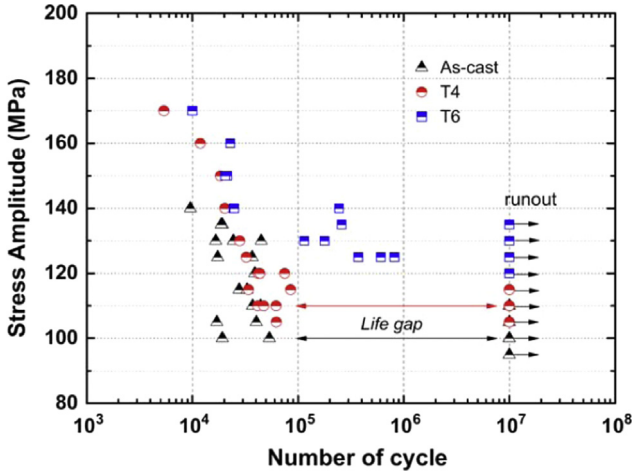

Fig. 11. S–N curves of the as-cast Mg–Gd–Zn–Zr alloys: black triangles: the as-cast alloy; Red circle: the solution treated alloy (T4); and Blue square: solution and artificial aged alloy (T6). Reproduced from Refs. [71,72].

Mg alloys having a better corrosion resistance compared with the conventional Mg alloys such as AZ31, WE43, ZK60 and ZX60 [73–79]. Izumi et al. [73] reported that the LPSO containing Mg–Zn–Y alloys exhibited the excellent corrosion performance and ascribed this to the passivity and the improvement of resistance to local breakdown of the films due to the combination effects of Al addition and rapid solidification [73]. Zhao et al. compared the mechanical properties and corrosion behavior of warm extruded LPSO containing $Mg_{99.83}Zn_1Y_2Zr_{0.17}$ alloy with those of the conventional alloys (AZ31, WE43, ZK60 and EX60), and found that the former exhibited a better combination of mechanical strength and corrosion performance [75]. However, Zhang et al. reported that the corrosion behavior of Mg–Zn–Y alloys depended on not only the volume fraction of LPSO phase, but also their distribution and morphology [76]. It revealed that the net-like continuous distribution and an appropriate volume fraction (moderate) of LPSO phase could ensure the alloy having the lowest corrosion rate [76]. Wang et al. [77] compared the corrosion potential (E_{corr}) of an Al-containing Mg alloy (Mg_{96}–Zn_1Y_2–Al_1) with those of Al-free Mg alloy (Mg_{96}–Zn_1Y_2) and relatively less Al content alloy ($Mg_{96.5}$–Zn_1Y_2–$Al_{0.5}$), and found that the E_{corr} value of the former alloy was lower than those of the latter two. It firmly indicates that the addition of Al can increase the corrosion resistance of the LPSO containing Mg alloys.

Okouchi et al. investigated the corrosion behavior of both Mg–Zn–Y–Al alloys containing with and without LPSO phases, and found that the corrosion rate of the alloy with LPSO phase was 1.5 times lower than that of the alloy containing without LPSO phase [78].

6. Biodegradation behavior of LPSO phase containing Mg alloys

Due to the similar strength to the natural bone and better biocompatibility, many efforts have been made for developing the biodegradable Mg-based alloys as the implant materials for the cardiovascular and orthopedic applications. So far, lots of scientific and technological articles have been published [79–85], and several comprehensive review articles about bio-degradation of Mg alloys can also be referred [79–81].

Zhao et al. investigated the bio-degradation behavior of the as-extruded LPSO containing Mg–Zn–Y–Zr alloy, and found that the

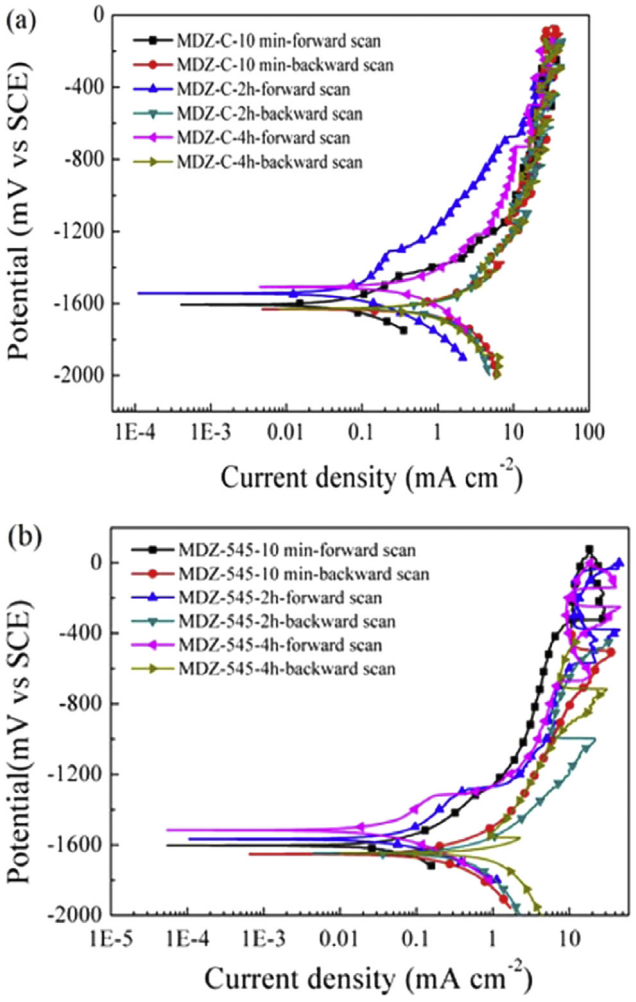

Fig. 12. Cyclic polarization curves of Mg alloys with 18R (a), and 14H LPSP (b) phases in 0.9 wt% NaCl solution after immersing for 10 min, 2 h and 4 h, respectively [84].

alloy exhibited a good combination of high mechanical strength, lower biodegradation rate and better biocompatibility [82]. However, with increasing in the volume fraction of LPSO phase, the biodegradation rate of the alloy was accelerated [83]. Moreover, Zhao et al. proposed that the biodegradation behavior of Mg alloys both in vitro and vivo was dominated by their corrosion mechanism [82,83]. Although the formation of LPSO phases in Mg alloys can decrease the degradation rate, the corrosion mechanisms of different LPSO structures were different [84]. Peng et al. compared the cyclic polarization behaviors of Mg-alloy with 18R- and 14H-LPSO phases in 0.9 wt% NaCl solution after immersing for different time [84], as shown in Fig. 12. It was found that the I_{corr} value of the 18R-LPSO containing alloy increased with immersion time, leading to a larger ACR value, whereas, a relative stable I_{corr} and ACR values could be maintained for the alloy containing with 14H. These observations show that for the Mg alloy containing with 18R, the porous bands distributed along the grain boundaries extended with the preceding of the degradation process and the surface oxidation film was broken down during polarization test. However, for the 14H-LPSO containing alloy only some isolated pitting spots occurred during cyclic polarization test.

7. Future trends

So far, the formation and microstructural evolution in LPSO-containing Mg alloys, as well as their effects on the mechanical and corrosion properties at both room and elevated temperatures have been briefly reviewed in this article. Recently, besides the LPSO-containing Mg alloys, the formation of quasi crystalline phases (I-phase) and their effect on the service properties of Mg alloys is another hot research topic [85–107]. Previous work demonstrated that the formation of I-phase particles in the matrix can also be beneficial for improving the mechanical strength, fracture toughness, corrosion resistance and fatigue strength of Mg alloys [85–89,91–92,101–103]. Compared with these two alloys, they are all the promising high-strength rare-earth containing Mg alloys for the potential engineering applications. However, since the deformation kink can occur in the LPSO structures during various kinds of deformation modes, the LPSO-containing Mg alloys can not only have high-strength, but also have a remarkable deformability with compression strains up to 60% [16,43,49,50]. Therefore, LPSO-containing Mg alloys could be more suitable for the plastic forming process of final products. Based on the referred research work mentioned above, however, some scientific questions have still not been satisfactorily answered. Here, we just make several conclusions and point out some areas that would be worthwhile for further scientific investigation in the future.

(1) Although there are five types of LPSO phases (6H, 10HR, 14H, 18R and 24R) existed in ternary system alloys of Mg–Zn–RE (RE=rare elements), Mg–Y–TE (TE=Cu and Ni), and quaternary system alloys such as Mg–Y–Gd–Zr and Mg–Y–Zn–Zr, Mi et al. reported that some new kinds of LPSO structures (15R, 12H and 21R) can still be observed in Mg alloys [11]. It is reasonable to anticipate that besides these eight kinds of LPSO phases (6H, 10HR, 14H, 18R, 24R, 15R, 12H and 21R) mentioned above, some new types of LPSO structures can probably be observed in the newly developed or processed Mg alloys. Therefore, the systematically investigation about the formation conditions for LPSO phases and the determinant factors for their structural variation are quite essential to be further carried out.

(2) To obtain the key factors for determining the order structure of LPSO phases, besides considering the stacking and chemical order along c-axis of LPSO structures, the in-plane orders of different types of LPSO structures are also needed to be clarified. Moreover, more emphases should be put on the electronic structures, atomic radius, mixing enthalpy of the LPSO containing Mg alloys.

(3) Although lot s of research work demonstrate that LPSO structure can have a positive effect on the properties of the alloys, the associated mechanism are quite complicated such as their structure, size, morphology, distribution and volume fraction and etc. In this aspect, a systematic work in-depth is still of absence, in particular, the effect of LPSO phase on fatigue behavior of the alloy is quite limited. Generally, the design criteria for the alloy development require the materials to have a better combined mechanical property. Therefore, the extensive researches about the mechanism for property improvement due to the presence of LPSO phases and their effect on fatigue behavior are still needed to be deeply carried out.

(4) Previous work indicates that LPSO phase can be helpful for improving the corrosion resistance of Mg alloys. However, further studies demonstrate that the corrosion properties of LPSO containing Mg alloys are related to the distribution, morphology and volume fraction of LPSO phases. As for whether it has a critical requirement for their existing state to ensure a better corrosion resistance, so far, no relevant research work can be referred. Therefore, deep investigations are still needed to be further performed as for the effect of LPSO phase on the corrosion behavior of Mg alloys.

(5) Currently, Mg alloys being used as biodegradable implant

materials become one of the hottest topics. Although the LPSO-containing Mg alloys can have excellent properties in terms of mechanical properties and corrosion resistance, their application for the implant materials requires the excellent combined properties, including biocompatibility, mechanical properties, and corrosion performance as well as the better loading-bearing capability [79]. Therefore, the future work about the application of the LPSO-containing alloys being as the biomaterials should focus on the improvement of their combined properties.

Acknowledgments

This work was supported by the National Natural Science Foundation of China Grant nos. 51271183, 51171192 and 51301172, the National Basic Research Program of China (973 Program) project under Grant no. 2013CB632205, and the Innovation Fund of Institute of Metal Research (IMR), Chinese Academy of Sciences (CAS). Special thanks to Professor X.H. Shao from IMR, CAS for her helpful suggestions and modifications to this manuscript.

References

[1] Y. Kawamura, K. Hayashi, A. Inoue, T. Masumoto, Mater. Trans. 42 (2001) 1172–1176.
[2] E. Abe, Y. Kawamura, K. Hayashi, A. Inoue, Acta. Mater. 50 (2002) 3845–3857.
[3] Y. Kawamura, T. Kasahara, S. Izumi, M. Yamasaki, Scr. Mater. 55 (2006) 453–456.
[4] A. Inoue, Y. Kawamura, M. Matsushita, K. Hayashi, J. Koike, J. Mater. Res. 16 (2001) 1894–1900.
[5] Z. Luo, S. Zhang, J. Mater. Sci. Lett. 19 (2000) 813–815.
[6] Z. Luo, S. Zhang, Y. Tang, D. Zhao, J. Alloy. Compd. 209 (1994) 275–278.
[7] T. Itoi, T. Seimiya, Y. Kawamura, M. Hirohashi, Scr. Mater. 51 (2004) 107–111.
[8] M. Matsuda, S. Ii, Y. Kawamura, Y. Ikuhara, M. Nishida, Mater. Sci. Eng. A. 393 (2005) 269–274.
[9] A. Ono, E. Abe, T. Itoi, M. Hirohashi, M. Yamasaki, Y. Kawamura, Mater. Trans. 49 (2008) 990–994.
[10] S.B. Mi, Q.Q. Jin, Scr. Mater. 68 (2013) 635–638.
[11] Y. Zhu, A. Morton, J. Nie, Acta. Mater. 58 (2010) 2936–2947.
[12] E. Abe, A. Ono, T. Itoi, M. Yamasaki, Y. Kawamura, Philos. Mag. Lett. 91 (2011) 690–696.
[13] X.H. Shao, H.J. Yang, J. De Hosson, X.L. Ma, Microsc. Microanal. 19 (2013) 1575–1580.
[14] Y.M. Zhu, A. Morton, J.F. Nie, Acta Mater. 60 (2012) 6562–6572.
[15] Y. Kawamura, M. Yamasaki, Mater. Trans. 48 (2007) 2986–2992.
[16] X.H. Shao, Z.Q. Yang, X.L. Ma, Acta Mater. 58 (2010) 4760–4771.
[17] G. Garces, E. Onorbe, F. Dobes, P. Perez, J.M. Antoranz, P. Adeva, Mater. Sci. Eng. A 539 (2012) 48–55.
[18] E. Onorbe, G. Garces, P. Perez, P. Adeva, J. Mater. Sci. 47 (2012) 1085–1093.
[19] E. Onorbe, G. Garces, F. Dobes, P. Perez, P. Adeva, Metall. Mater. Trans. A 44 (2013) 2869–2883.
[20] D.H. Ping, K. Hono, Y. Kawamura, A. Inoue, Philos. Mag. Lett. 82 (2002) 543–551.
[21] Q.Q. Jin, Institute of Metal Research, In: Chinese Academy Sciences, 2013.
[22] H. Kimizuka, M. Fronzi, S. Ogata, Scr. Mater. 69 (2013) 594–597.
[23] H. Yokobayashi, K. Kishida, H. Inui, M. Yamasaki, Y. Kawamura, Acta Mater. 59 (2011) 7287–7299.
[24] D. Egusa, E. Abe, Acta Mater. 60 (2012) 166–178.
[25] M. Yamasaki, M. Matsushita, K. Hagihara, H. Izuno, E. Abe, Y. Kawamura, Scr. Mater. 78–79 (2014) 13–16.
[26] T. Itoi, K. Takahashi, H. Moriyama, M. Hirohashi, Scr. Mater. 59 (2008) 1155–1158.
[27] A. Inoue, M. Matsushita, Y. Kawamura, K. Amiya, K. Hayashi, J. Koike, Mater. Trans. 43 (2002) 580–584.
[28] K. Amiya, T. Ohsuna, Mater. Trans. 44 (2003) 2151–2156.
[29] M. Matsuura, K. Konno, M. Yoshida, M. Nishijima, K. Hiraga, Mater. Trans. 47 (2006) 1264–1267.
[30] M. Yamasaki, T. Anan, S. Yoshimoto, Y. Kawamura, Scr. Mater. 53 (2005) 799–803.
[31] Y. Gao, Q.D. Wang, J.H. Gu, Y. Zhao, Y. Tong, D.D. Yin, J. Alloy. Compd. 477 (2009) 374–378.
[32] Y. Chino, M. Mabuchi, S. Hagiwara, H. Iwasaki, A. Yamamoto, H. Tsubakino, Scr. Mater. 51 (2004) 711–714.
[33] M. Yamasaki, M. Sasaki, M. Nishijima, K. Hiraga, Y. Kawamura, Acta Mater. 55 (2007) 6798–6805.
[34] K. Yamada, Y. Okubo, M. Shiono, H. Watanabe, S. Kamado, Y. Kojima, Mater. Trans. 47 (2006) 1066–1070.
[35] M. Matsuura, K. Konno, M. Yoshida, M. Nishijima, K. Hiraga, Mater. Trans. 47 (2006) 1264–1267.
[36] J.E. Saal, C. Wolverton, Scr. Mater. 67 (2012) 798–801.
[37] J. Grobner, A. Kozlov, X.Y. Fang, J. Geng, J.F. Nie, R. Schmid-Fetzer, Acta Mater. 60 (2012) 5948–5962.
[38] X. Shao, Z. Yang, J. You, K. Qiu, X. Ma, J. Alloy. Compd. 509 (2011) 7221–7228.
[39] P. Apps, H. Karimzadeh, J. King, G. Lorimer, Scr. Mater. 48 (2003) 1023–1028.
[40] A. Datta, U.V. Waghmare, U. Ramamurty, Acta Mater. 56 (2008) 2531–2539.
[41] Q.Q. Jin, C.F. Fang, S.B. Mi, J. Alloy. Compd. 568 (2013) 21–25.
[42] H. Yokobayashi, K. Kishida, H. Inui, M. Yamasaki, Y. Kawamura, Mater. Res. Soc. Symp. Proc. (2011), http://dx.doi.org/10.1557/opl.2011.1536.
[43] K. Hagihara, N. Yokotani, Y. Umakoshi, Intermetallics 18 (2010) 267–276.
[44] T. Horiuchi, A. Ono, K. Yoshioka, T. Watanabe, K. Ohkubo, S. Miura, T. Mohri, S. Tamura, Mater. Trans. 49 (2008) 2247–2253.
[45] J.E. Saal, C. Wolverton, Acta Mater. 68 (2014) 325–338.
[46] G. Garcés, P. Pérez, S. González, P. Adeva, Int. J. Mater. Res. 97 (2006) 404–408.
[47] K. Kishida, H. Yokobayashi, H. Inui, M. Yamasaki, Y. Kawamura, Intermetallics 31 (2012) 55–64.
[48] Q.-Q. Jin, S.-B. Mi, Intermetallic phases in Mg–Co–Y alloys, J. Alloy. Compd. 582 (2014) 130–134.
[49] K. Hagihara, A. Kinoshita, Y. Sugino, M. Yamasaki, Y. Kawamura, H. Yasuda, Y. Umakoshi, Intermetallics 18 (2010) 1079–1085.
[50] K. Hagihara, A. Kinoshita, Y. Sugino, M. Yamasaki, Y. Kawamura, H.Y. Yasuda, Y. Umakoshi, Acta Mater. 58 (2010) 6282–6293.
[51] J. Hess, C. Barrett, Trans. AIME 185 (1949) 599–606.
[52] M.W. Barsoum, L. Farber, T. El-Raghy, Metall. Mater. Trans. A 30 (1999) 1727–1738.
[53] D. Egusa, M. Yamasaki, Y. Kawamura, E. Abe, Mater. Trans. 54 (2013) 698–702.
[54] M. Matsuda, S. Ii, Y. Kawamura, Y. Ikuhara, M. Nishida, Mater. Sci. Eng. A 386 (2004) 447–452.
[55] X.H. Shao, Z.Q. Yang, X.L. Ma, Philos. Mag. Lett. 94 (2014) 150–156.
[56] J.F. Nie, Y.M. Zhu, J.Z. Liu, X.Y. Fang, Science 340 (2013) 957–960.
[57] B.J. Lv, J. Peng, Y. Peng, A.T. Tang, F.S. Pan, Mater. Sci. Eng. A 579 (2013) 209–216.
[58] B.J. Lv, J. Peng, Ll Zhu, Y.J. Wang, A.T. Tang, Mater. Sci. Eng. A 599 (2014) 150–159.
[59] M. Ryo, M. Yamasaki, M. Otsu, Mater. Trans. 50 (2009) 841–846.
[60] M. Yamasaki, K. Hashimoto, K. Hagihara, Y. Kawamura, Acta Mater. 59 (2011) 3646–3658.
[61] T. Laser, C. Hartig, M. Nürnberg, D. Letzig, R. Bormann, Acta Mater. 56 (2008) 2791–2798.
[62] Y. Jono, M. Yamasaki, Y. Kawamura, Mater. Trans. 54 (2013) 703–712.
[63] M.M. Avedesian, H. Baker, ASM Spec. (1999) 258.
[64] K. Hagihara, A. Kinoshita, Y. Fukusumi, M. Yamasaki, Y. Kawamura, Mater. Sci. Eng. A 560 (2013) 71–79.
[65] Y. Chino, M. Kado, M. Mabuchi, Acta Mater. 56 (2008) 387–394.
[66] S.M. Fatemi-Varzaneh, A. Zarei-Hanzaki, M. Haghshenas, Mater. Sci. Eng. A 497 (2008) 438–444.
[67] K. Ishikawa, H. Watanabe, T. Mukai, Mater. Lett. 59 (2005) 1511–1515.
[68] A. Galiyev, R. Kaibyshev, G. Gottstein, Acta Mater. 49 (2001) 1199–1207.
[69] Y. Zhang, X.Q. Zeng, C. Lu, W.J. Ding, Mater. Sci. Eng. A 428 (2006) 91–97.
[70] Y. Mine, H. Yoshimura, M. Matsuda, K. Takashima, Y. Kawamura, Mater. Sci. Eng. A 570 (2013) 63–69.
[71] Z.L. He, P.H. Fu, Y. Wang, X. Xu, W. Ding, Mater. Sci. Eng. A 587 (2013) 72–78.
[72] Z. He, L. Peng, P. Fu, Y. Wang, X. Hu, W. Ding, Mater. Sci. Eng. A 604 (2014) 78–85.
[73] S. Izumi, M. Yamasaki, Y. Kawamura, Corros. Sci. 51 (2009) 395–402.
[74] M. Yamasaki, S. Izumi, Y. Kawamura, H. Habazaki, Appl. Surf. Sci. 257 (2011) 8258–8267.
[75] X. Zhao, L.L. Shi, J. Xu, Mater. Sci. Eng. C 33 (2013) 3627–3637.
[76] J. Zhang, J. Xu, W. Cheng, C. Chen, J. Kang, J. Mater. Sci. Technol. 28 (2012) 1157–1162.
[77] D. Wang, J.S. Zhang, J.D. Xu, Z.L. Zhao, W.L. Cheng, C.X. Xu, J. Magnes. Alloy. 2 (2014) 78–84.
[78] H. Okouchi, Y. Seki, T. Sekigawa, H. Hira, Y. Kawamura, Mater. Sci. Forum 638–642 (2010) 1476–1481.
[79] Y.J. Chen, Z.G. Xu, C. Smith, J. Sankar, Acta. Biomater. 10 (2014) 4561–4573.
[80] M.P. Staiger, A.M. Pietak, J. Huadmai, G. Dias, Biomater 27 (2006) 1728–1734.
[81] N.T. Kirkland, N. Birbilis, M.P. Staiger, Biomater 8 (2012) 925–936.
[82] X. Zhao, L.L. Shi, J. Xu, Mater. Sci. Eng. C 33 (2013) 3627–3637.
[83] X. Zhao, L.L. Shi, J. Xu, J. Mech. Behav. Biomed. Mater. 18 (2013) 181–190.
[84] Q. Peng, J.X. Guo, H. Fu, X.C. Cai, Y.A. Wang, B.Z. Liu, Z.G. Xu, Sci. Rep. (2014), http://dx.doi.org/10.1038/srep 03620.
[85] D.K. Xu, L. Liu, Y.B. Xu, E.H. Han, Acta Mater. 56 (2008) 985–994.
[86] A. Singh, M. Nakamura, M. Watanabe, A. Kato, A.P. Tsai, Scr. Mater. 49 (2003) 417–422.
[87] D.K. Xu, C.Q. Li, B.J. Wang, E.H. Han, Mater. Des. 88 (2015) 88–97.
[88] C.Q. Li, D.K. Xu, T.T. Zu, E.H. Han, L. Wang, J. Magnes. Alloy. 3 (2015) 106–111.
[89] D.K. Xu, B.J. Wang, C.Q. Li, T.T. Zu, E.H. Han, Mater. Des. 69 (2015) 124–129.
[90] S.D. Wang, D.K. Xu, X.B. Chen, E.H. Han, C. Dong, Corros. Sci. 92 (2015) 228–236.
[91] D.K. Xu, E.H. Han, Scr. Mater. 71 (2014) 21–24.
[92] D.K. Xu, T.T. Zu, M. Yin, E.H. Han, J. Alloy. Compd. 582 (2013) 161–166.

[93] D.K. Xu, E.H. Han, Progress in Natural Science, Mater. Int. 22 (2012) 364–385.
[94] J.Y. Lee, H.K. Lim, D.H. Kim, W.T. Kim, D.H. Kim, Effect of volume fraction of qusicrystal on the mechanical properties of quasicrystal-reinforced Mg–Zn–Y alloys, Mater. Sci. Eng. A 449–451 (2007) 987–990.
[95] D.K. Xu, W.T. Tang, L. Liu, Y.B. Xu, E.H. Han, J. Alloy. Compd. 432 (2007) 129–134.
[96] D.K. Xu, L. Liu, Y.B. Xu, E.H. Han, J. Alloy. Compd. 426 (2006) 155–161.
[97] J.Y. Lee, D.H. Kim, H.K. Lim, D.H. Kim, Mater. Lett. 59 (2005) 3801–3805.
[98] D.K. Xu, L. Liu, Y.B. Xu, E.H. Han, Mater. Sci. Eng. A 443 (2007) 248–256.
[99] Y. Zhang, X.Q. Zeng, L.F. Liu, C. Lu, H.T. Zhou, Q. Li, Y.P. Zhu, Mater. Sci. Eng. A 373 (2004) 320–327.
[100] D.K. Xu, W.T. Tang, L. Liu, Y.B. Xu, E.H. Han, J. Alloy. Compd. 461 (2008) 248–252.
[101] J.S. Zhang, L.X. Pei, H.W. Du, W. Liang, C.X. Xu, B.F. Lu, J. Alloy. Compd. 453 (2008) 309–315.
[102] E. Mora, G. Garce's, E. Onorbe, P. Pe'rez, P. Adeva., Scr. Mater. 60 (2009) 776–779.
[103] D.K. Xu, L. Liu, Y.B. Xu, E.H. Han, Scr. Mater. 57 (2007) 285–288.
[104] D.K. Xu, L. Liu, Y.B. Xu, E.H. Han, J. Alloy. Compd. 431 (2007) 107–111.
[105] D.K. Xu, L. Liu, Y.B. Xu, E.H. Han, Acta Metall. Sin. 43 (2007) 144–148.
[106] D.K. Xu, L. Liu, Y.B. Xu, E.H. Han, J. Alloy. Compd. 454 (2008) 123–128.
[107] D.K. Xu, L. Liu, Y.B. Xu, E.H. Han, Metall. Mater. Trans. A 40 (2009) 1727–1740.

Dr. En-Hou Han is the full professor, Director of National Engineering Center for Corrosion Control and Environmental Corrosion Center, Director of CAS Key Lab for Nuclear materials and Safety Assessment the Institute of Metal Research, Chinese Academy of Sciences (CAS). He received Fellow of NACE International in 2008. He has published more than 400 peer reviewed scientific papers, 77 plenary and invited lecture, and hold 72 patents. His papers were cited more than 5000 times. His research interests include (1) development of advanced magnesium alloy and its corrosion prevention techniques. (2) Corrosion and stress corrosion of materials in nuclear power plant and nuclear waste disposal. (3) R & D of various coatings, such as nano-composite coatings and nano-composite plating. (4) Interaction of mechanics and chemistry, including stress corrosion cracking, corrosion fatigue and hydrogen embrittlement for various materials. (5) Corrosion in severe corrosive industrial environments, e.g., high temperature and high-pressure, H_2S, acidic or alkaline environments. (6) Service lifetime prediction and failure analysis for engineering structure and components.